

# Quadrupole spin polarization as signature of second-order topological superconductors

Kirill Plekhanov,<sup>1</sup> Niclas Müller,<sup>2</sup> Yanick Volpez,<sup>1</sup> Dante M. Kennes,<sup>2,3</sup> Herbert Schoeller,<sup>2</sup> Daniel Loss,<sup>1</sup> and Jelena Klinovaja<sup>1</sup>

<sup>1</sup>*Department of Physics, University of Basel, Klingelbergstrasse 82, CH-4056 Basel, Switzerland*

<sup>2</sup>*Institut für Theorie der Statistischen Physik, RWTH Aachen, 52056 Aachen, Germany and JARA - Fundamentals of Future Information Technology*

<sup>3</sup>*Max Planck Institute for the Structure and Dynamics of Matter and Center for Free-Electron Laser Science, 22761 Hamburg, Germany*

(Dated: August 11, 2020)

We study theoretically second-order topological superconductors characterized by the presence of pairs of zero-energy Majorana corner states. We uncover a quadrupole spin polarization at the system edges that provides a striking signature to identify topological phases, thereby complementing standard approaches based on zero-bias conductance peaks due to Majorana corner states. We consider two different classes of second-order topological superconductors with broken time-reversal symmetry and show that both classes are characterized by a quadrupolar structure of the spin polarization that disappears as the system passes through the topological phase transition. This feature can be accessed experimentally using spin-polarized scanning tunneling microscopes. We study different models hosting second-order topological phases, both analytically and numerically, and using Keldysh techniques we provide numerical simulations of the spin-polarized currents probed by scanning tips.

*Introduction.* Over the last two decades, topological insulators (TIs) and superconductors (TSCs) have become a subject of wide interest in condensed matter physics [1–8]. One of the main attractions of such systems is the existence of topologically protected gapless  $(d-1)$ -dimensional modes which emerge at the boundary of a topologically nontrivial  $d$ -dimensional bulk – a phenomenon known as bulk-boundary correspondence. The topological nature of the boundary modes makes them insensitive to external perturbations and disorder, which is of great importance in the context of quantum computing [9–11]. Recently, the concept of bulk-boundary correspondence has been generalized to a new class of systems, called higher-order topological insulators and superconductors [12–15]. In contrast to conventional topological systems, the  $(d-1)$ -dimensional boundary of an  $n$ -th order TI/TSC is gapped. Instead, it exhibits protected gapless modes on  $(d-n)$ -dimensional boundaries. The corresponding gapless modes are called corner states in the case  $n = d \geq 2$ .

Pioneering theoretical works on higher-order TIs have been followed by fast progress from the experimental side [16–26]. Particular attention has been dedicated to theoretical investigations of TSCs that host Majorana corner states (MCSs) – Majorana bound states (MBSs) located at the corners of the system [27–49]. Nevertheless, the experimental realization of such systems remains challenging. Usual protocols to detect MBSs in (higher-order) TSCs are based on a direct state tomography or detection of specific features, such as a zero-bias peak in the differential conductance. However, such probes do not provide a clear way to distinguish between MBSs and other types of bound states of topologically trivial nature [50–64], which hinders unambiguous identification of the topological phases and calls for additional experimental signatures.

In this work, we propose a solution to the problem described above, based on an alternative probe of second-order TSCs (SOTSCs) with broken time-reversal symmetry, which can be implemented with the help of scanning tunneling microscopes (STMs) [65–73]. We consider a subclass of SOTSCs represented by two simple models: the first one supports two MCSs at a single pair of two opposite corners and the second one supports four MCSs – one at every corner of the setup. The topological phase transition in such systems is accompanied by a drastic change in the spin polarization structure at the system edges, which we denote as a quadrupolar structure of the spin polarization. The analytical arguments justifying the emergence of such edge features are confirmed numerically. We then provide results of numerical simulations of the current flowing between a local spin-polarized probe (an STM tip) and the sample, making use of Keldysh techniques. We expect that our approach can also be applied to probe other higher-order topological phases with broken time-reversal symmetry. Importantly, the proposed signatures are stable against weak disorder and do not rely on any other symmetry than the particle-hole symmetry of the superconductor.

*SOTSCs with two corner states.* To begin with, we consider a SOTSC which supports a single pair of corner states [27–34]. The starting point of our consideration is a simple 2D model for a helical TSC [32], described by the following Hamiltonian in momentum representation:

$$\mathcal{H}_0(\mathbf{k}) = 2t [2 - \cos(k_x a) - \cos(k_y a)] \eta_z - \mu_0 \eta_z + \Gamma \eta_z \tau_x + \alpha [\sin(k_y a) \sigma_x - \sin(k_x a) \eta_z \sigma_y] \tau_z + \Delta_{sc} \eta_y \sigma_y \tau_z. \quad (1)$$

The Pauli matrices  $\eta_j$  act on the particle-hole space,  $\sigma_j$  – on the spin space, and  $\tau_j$  – on a generic local degree of freedom (e.g. an electron orbital). We work in the Nambu basis  $(\psi_{\uparrow 1}, \psi_{\downarrow 1}, \psi_{\uparrow 1}^\dagger, \psi_{\downarrow 1}^\dagger, \psi_{\uparrow \bar{1}}, \psi_{\downarrow \bar{1}}, \psi_{\uparrow \bar{1}}^\dagger, \psi_{\downarrow \bar{1}}^\dagger)$ ,

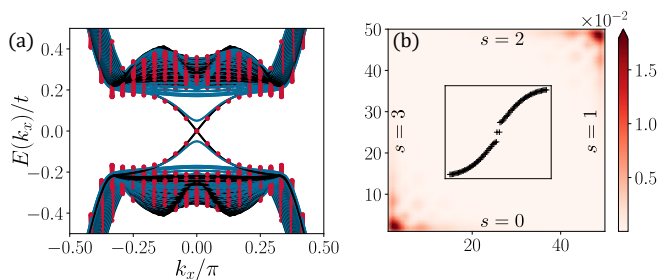


FIG. 1. (a) Spectrum of  $\mathcal{H}$  calculated in a geometry with OBC along the  $y$  axis for  $\Delta_z = 0$  (black lines),  $\Delta_z = 0.05t$  and  $\theta_z = 0$  (blue lines), as well as  $\Delta_z = 0.05t$  and  $\theta_z = \pi/2$  (red dots). We see that only the  $x$  component of the Zeeman field gaps out the helical edge modes, which are present in the system when  $\Delta_z = 0$ . (b) Probability density of the MCSs calculated in a geometry with OBCs along both  $x$  and  $y$  axis for  $\Delta_z = 0.05t$  and  $\theta_z = \pi/4$ . The inset shows the low-energy spectrum. All the simulations are performed in the topological regime of the phase diagram with  $\Gamma = 2\Delta_{sc} = \alpha = 0.5t$ ,  $\mu_0 = 0$ , and  $a = 1$ .

where  $\psi_{\sigma\tau}^\dagger$  creates an electron of species  $\tau$  and spin  $\sigma$ . The parameters  $\Delta_{sc}$  and  $\mu_0$  describe the  $s$ -wave superconducting pairing amplitude and the chemical potential, respectively, while  $t$ ,  $\alpha$  as well as  $\Gamma$  depend on the microscopic details of the system and  $a$  is the lattice constant (see Supplemental Material (SM) [76] for more details). The proposed model is characterized by a topological phase transition at  $\Gamma = \Delta_{sc}$ . The region  $\Gamma < \Delta_{sc}$  is trivial, while  $\Gamma > \Delta_{sc}$  corresponds to a helical TSC, supporting a pair of gapless edge modes. The existence of these edge modes is protected by the time-reversal symmetry  $T = i\sigma_y K$ , obeying  $T\mathcal{H}_0(\mathbf{k})T^{-1} = \mathcal{H}_0(-\mathbf{k})$ , with  $K$  being the complex conjugation operator. The topological phase diagram can be checked numerically in a geometry with open boundary condition (OBC) along one fixed direction [see Fig. 1(a)]. The resulting spectrum is independent of the particular choice of the OBC direction as a result of the in-plane rotational symmetry present in the system.

The helical edge modes can be gapped out by applying an external Zeeman field, which breaks time-reversal symmetry. The corresponding contribution to the Hamiltonian can be expressed as

$$\mathcal{H}_z = \Delta_z [\cos(\theta_z)\eta_z\sigma_x + \sin(\theta_z)\sigma_y], \quad (2)$$

where  $\Delta_z$  ( $\theta_z$ ) defines the strength (in-plane orientation) of the Zeeman field. The total Hamiltonian then becomes  $\mathcal{H}(\mathbf{k}) = \mathcal{H}_0(\mathbf{k}) + \mathcal{H}_z$ . One can easily show both numerically and analytically that edge modes are gapped out only by the Zeeman field component that is parallel to the edge, see Fig. 1(a). As a result, the rotational symmetry is broken down to the inversion symmetry  $I = \eta_z\tau_x$ , which satisfies  $I\mathcal{H}(\mathbf{k})I^{-1} = \mathcal{H}(-\mathbf{k})$ . When the Zeeman field is smaller than the bulk gap of the TSC,  $\Delta_z \ll |\Gamma - \Delta_{sc}|$ , the boundary physics of the system away from the corners is described by a  $2 \times 2$

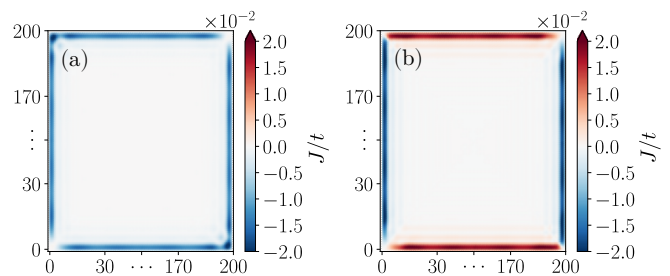


FIG. 2. Numerical calculations of the current  $J$  through the spin-polarized STM tip for a system described by  $\mathcal{H}$  given below Eq. (2). The polarization of the STM is chosen to be in-plane (a) parallel to the Zeeman field and (b) perpendicular to the Zeeman field. The out-of-plane component is trivially zero. We see that while the parallel component of the polarization is roughly constant and negative along the entire boundary, the perpendicular component has a quadrupolar structure, *i.e.* changes sign on every edge. The parameters of the simulation are  $\Gamma = 1.75\Delta_{sc} = 0.44t$ ,  $\Delta_z = 0.05t$ ,  $\kappa = 2.5 \cdot 10^{-4}t$ , and the contribution to the current is summed over  $V$  from 0 to  $\Delta_z$ .

Jackiw-Rebbi Hamiltonian [74, 75]

$$\mathcal{H}_{\text{eff},s}(k_s) = v_F k_s \rho_z - m_s \rho_y, \quad (3)$$

where  $\rho_j$  act on the space of helical states  $|\Psi_{0,\pm}^s\rangle$  belonging to the edge  $s \in \{0, 1, 2, 3\}$  [see Fig. 1(b)],  $k_s$  denotes the momentum parallel to the edge,  $v_F$  the Fermi velocity. The strength of the mass term is given by  $m_s = \Delta_z \cos(\theta_z - \theta_s)$  with  $\theta_s = s\pi/2$  (see SM [76]). We denote by  $|\Psi_{0,+}^s\rangle$  ( $|\Psi_{0,-}^s\rangle$ ) the states which move clockwise (anticlockwise). Most importantly, as a result of the presence of the inversion symmetry, opposite edges are necessarily described by opposite signs of the mass term  $m_s$  (*i.e.*  $m_0 = -m_2$  and  $m_1 = -m_3$ ). Consequently, in a finite-size geometry where  $m_s$  is finite on every edge, there exist two corners connecting two edges with opposite signs of  $m_s$ . Such gap inversion corners host zero-energy states identified with MCSs of a SOTSC. Numerical evidence of the existence of MCSs is shown in Fig. 1(b). We note that such a SOTSC phase remains stable against arbitrary types of disorder as long as additional perturbations do not close the surface gap [28–30].

*Quadrupolar structure of  $\langle S_\perp \rangle$ .* At low energies, the physics of the setup is dictated by the Zeeman term. In particular, the eigenstates of  $\mathcal{H}_{\text{eff},s}$  at  $k_s = 0$  become spin-polarized and acquire the form

$$|\Psi_\pm^s\rangle = (|\Psi_{0,+}^s\rangle \mp i \text{sgn}(m_s) |\Psi_{0,-}^s\rangle) / \sqrt{2}. \quad (4)$$

The states  $|\Psi_\pm^s\rangle$  correspond to the eigenvalues  $\pm|m_s|$  and have the spin polarization  $\langle \Psi_\pm^s | S_\parallel | \Psi_\pm^s \rangle = \pm|m_s|/\Delta_z$ , where  $S_\parallel$  is the spin operator along the direction of the Zeeman field. Similarly, one can calculate the expectation values of the in-plane polarization perpendicular to the applied Zeeman field, associated with the operator  $S_\perp$ . In our case, we use the rotational symmetry of  $\mathcal{H}_0$  and notice that the gapless states at the

edge  $s - 1$  (where we identify  $-1$  with  $3$ ) are related to the gapless states at the edge  $s$  via a  $\pi/2$ -rotation (see SM [76]). Hence, the expectation values of  $S_{\perp}$  in the basis of states  $|\Psi_{0,\pm}^s\rangle$  is exactly equal to the expectation values of  $S_{\parallel}$  in the basis  $|\Psi_{0,\pm}^{s-1}\rangle$ , resulting in  $\langle\Psi_{\pm}^s|S_{\perp}|\Psi_{\pm}^s\rangle = \pm\text{sgn}(m_s)m_{s-1}/\Delta_z$ . Taking into account that, restricted by the inversion symmetry, the sign of  $m_s$  changes on every second edge, the sign of the perpendicular component of the spin polarization of low-energy states changes on every edge. We refer to this feature as the quadrupolar structure of the spin polarization.

In Fig. 2 we present the results of a numerical calculation of the spin polarization, based on the Keldysh formalism [68]. We mimic the STM measurement [69–73] by coupling the system to a spin-polarized tip with an amplitude  $\kappa$ . We then calculate the current  $J$  that flows between the system and the tip by summing up the contribution of the states in the energy window  $[-V, 0]$  (see SM [76]), where  $V$  corresponds to the bias voltage of the STM tip. We consider two directions of the tip polarization: one parallel and one perpendicular to the Zeeman field. As expected from the analytical argument at  $k_s = 0$ , we find that in the topological regime, the expectation value of  $S_{\parallel}$  is roughly constant and negative, while for  $S_{\perp}$  it changes sign on every edge. These features are characteristic for the SOTSCs close to the topological phase transition.

We note that the magnitude of spin polarization may depend on the properties of the states  $|\Psi_{0,\pm}^s\rangle$  and the symmetries of  $\mathcal{H}_0$  (see SM [76] for a more detailed study including the calculation of the quadrupolar moment across the phase transition). Nevertheless, the quadrupolar structure associated with the sign of the spin polarization at different edges depends only on the sign of  $m_s$ , which are topologically protected quantities. Hence, observing a quadrupolar structure of the spin-polarization provides a prominent and unique signature of the system topology. Moreover, the effective edge Hamiltonian  $\mathcal{H}_{\text{eff},s}$  as well as the argument justifying the emergence of MCSs are generally valid for inversion-symmetric SOTSCs [27–30].

*SOTSCs with four corner states.* Next, we generalize our findings to a different class of SOTSCs and consider a SOTSC hosting a quadruplet of MCSs [35–44]. The basic ingredient of our construction here is a minimalist version of a 2D TI [3] proximity coupled to an  $s$ -wave superconductor with amplitude  $\Delta_{\text{sc}}$ . The corresponding Hamiltonian reads

$$\mathcal{H}'_0(\mathbf{k}) = \{\Gamma - 2t_x[1 - \cos(k_x a)] - 2t_y[1 - \cos(k_y a)]\}\eta_z\tau_z - \mu_0\eta_z + [\alpha_x \sin(k_x a)\sigma_x\tau_x - \alpha_y \sin(k_y a)\eta_z\tau_y] + \Delta_{\text{sc}}\eta_y\sigma_y, \quad (5)$$

where Pauli matrices  $\eta_j$ ,  $\sigma_j$ , and  $\tau_j$  play exactly the same role as in Eq. (1). The parameters  $t_x$ ,  $t_y$ ,  $\alpha_x$ ,  $\alpha_y$ , and  $\Gamma$  depend on the microscopic details of the system (see SM [76]). For  $\Delta_{\text{sc}} = 0$  the system is characterized by a

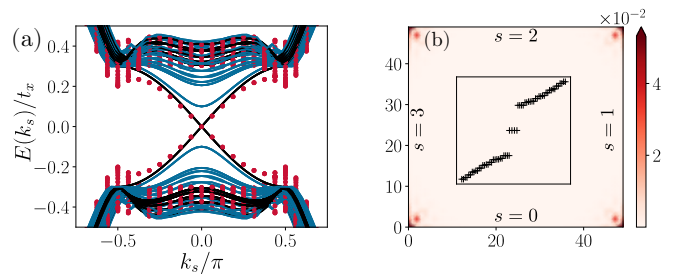


FIG. 3. (a) Spectrum of  $\mathcal{H}'$  for  $\Delta_{\text{sc}} = 0$ . When  $\Delta_z = 0$  (black lines), the system hosts a pair of gapless helical edge modes. A finite value of  $\Delta_z = 0.1t_x$  gaps out the edge modes in a geometry with OBC along the  $y$  axis (blue lines,  $k_s \equiv k_x$ ) but leaves the edge modes gapless in a geometry with OBC along the  $x$  axis (red dots,  $k_s \equiv k_y$ ). (b) Probability density of the MCSs calculated in a geometry with OBCs along both  $x$  and  $y$  axes in a topological regime of the phase diagram with  $\Delta_z = 2\Delta_{\text{sc}} = 0.1t_x$ . The inset shows the low-energy spectrum. The remaining parameters are  $\Gamma = t_y = t_x$ ,  $\alpha_x = \alpha_y = 0.3t_x$ ,  $\mu_0 = 0$ , and  $a = 1$ .

topological phase transition as a function of the parameter  $\Gamma$ . The closing of the gap occurs at  $\Gamma = 0$ , independently of the value of  $\alpha_x$  and  $\alpha_y$ . The region  $\Gamma < 0$  is topologically trivial, while  $\Gamma > 0$  is identified with a TI phase that supports gapless helical edge modes protected by the time-reversal symmetry  $T = i\sigma_y K$ . Again, we verify the presence of such edge modes by analyzing the model numerically in a geometry with OBC along one particular axis. The result of the calculation is shown in Fig. 3(a).

At non-zero  $\Delta_{\text{sc}}$ , the helical edge modes are gapped out. However, such a process acts identically on all the edges, transforming the system into a trivial superconductor. In order to achieve richer physics, one can apply the in-plane Zeeman field, described by the Hamiltonian term

$$\mathcal{H}'_z = \Delta_z \eta_z \sigma_x, \quad (6)$$

such that the total Hamiltonian becomes  $\mathcal{H}'(\mathbf{k}) = \mathcal{H}'_0(\mathbf{k}) + \mathcal{H}'_z$ . The resulting system is invariant under the inversion symmetry  $I = \tau_z$ . We also note that the exact orientation of the Zeeman field in the  $xy$  plane is not important, since the spectrum is invariant under an arbitrary rotation around the spin quantization axis. Interestingly, the effect of the in-plane Zeeman field alone differs strongly depending on the edge considered. This can be seen by considering two special lines in the momentum space, corresponding to vanishing  $k_x$  or  $k_y$ , which can be used to describe the physics of the system in a geometry with OBC along the  $y$  or  $x$  axis, respectively (see SM [76]). For  $k_y = 0$ , the Zeeman term leaves the edge modes gapless, while for  $k_x = 0$  it leads to an opening of the gap of the size  $\Delta_z$ . As a consequence, the modes propagating along  $x$ -edges of the system are gapped, while the ones along the  $y$ -edges remain gapless. The numerical verification of this feature is shown in Fig. 3(a).

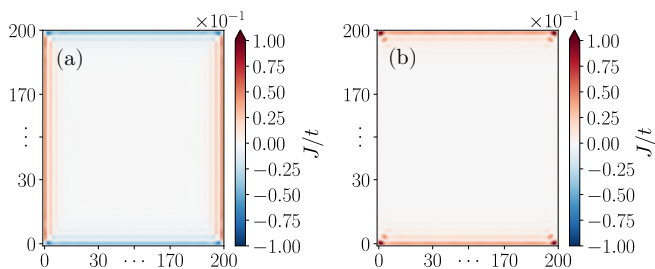


FIG. 4. Numerical calculation of the current  $J$  through the spin-polarized STM tip for a system described by  $\mathcal{H}'$  given below Eq. (6). The polarization of the STM is chosen to be parallel to the Zeeman field. (a) In the topological phase with  $\Delta_z = 1.75\Delta_{sc}$ , the polarization changes sign on every edge, resulting in a quadrupolar structure similar to the one of Fig. 2. (b) In the topologically trivial phase with  $\Delta_z = 0.25\Delta_{sc}$ , the polarization has the same sign along the entire system boundary. The signal is weaker along the  $y$ -edges because less edge states contribute in the energy window. The remaining parameters of the simulations are  $\Gamma = t_y = t_x$ ,  $\alpha_y = \alpha_x = 0.3t_x$ ,  $\Delta_{sc} = 0.1t_x$ ,  $\kappa = 5 \cdot 10^{-4}t_x$ . The current contributions are summed up over  $V = \Delta_{sc}$ .

By taking into account the effect of both the superconducting and Zeeman terms, one can construct the low-energy effective  $4 \times 4$  edge Hamiltonian, which reads

$$\mathcal{H}'_{\text{eff},s}(k_s) = v_F k_s \rho_z + m_s \eta_z \rho_x + \Delta_{sc} \eta_y \rho_y. \quad (7)$$

Here, we use the same convention as in Eq. (3) and denote by  $\rho_j$  the matrices acting on the states  $|\Psi'_{0,\pm}\rangle$ , associated with the right- and left-moving modes living on the edge  $s \in \{0, 1, 2, 3\}$  [see Fig. 3(b)]. The matrices  $\eta_j$  act in the particle-hole space and  $m_s$  denotes the mass originating from the Zeeman term. The mass vanishes on two  $y$ -edges:  $m_1 = m_3 = 0$ , while  $|m_0| = |m_2| = \Delta_z$  on two  $x$ -edges. Moreover, the effective description of every edge is identical to the low-energy physics of a topological nanowire [77–81], characterized by the topological phase transition at a critical point  $\Delta_z = \Delta_{sc}$ . Hence, if the Zeeman field is strong enough such that  $\Delta_z > \Delta_{sc}$ , the two  $x$ -edges of the system correspond to two wires in the topological regime, while the two  $y$ -edges – to two trivial nanowires. As a result, four corners of the system host four zero energy states, identified with MCSs. The regime  $\Delta_z < \Delta_{sc}$  is the topologically trivial phase. Similarly, the corner states disappear when the system moves into the trivial region of the phase diagram with  $\Gamma < 0$ . We also note that the topological description of the present model does not rely on the presence of the inversion symmetry  $I$ . Instead, the existence of four MCSs is ensured by a particular spatial structure of the gapping processes  $m_s$  and  $\Delta_{sc}$ , namely by the fact that one pair of opposite edges has  $|m_s| < \Delta_{sc}$ , while the other one has  $|m_s| > \Delta_{sc}$ .

*Quadrupolar structure of  $\langle S_{\parallel} \rangle$ .* We show that, again, a spin-polarized STM [68–73] can be used to probe the topological phase diagram of  $\mathcal{H}'_{\text{eff},s}$ . To show this, we consider the edges  $s = 0, 2$  and focus on the physics at the

Dirac point  $k_s = 0$ , where the phase transition occurs. We denote by  $|\Psi'_{\pm}\rangle$  two eigenstates of  $\mathcal{H}'_{\text{eff},s}$  associated with two lowest magnitude eigenvalues  $\pm|m_s - \Delta_{sc}|$ . The states  $|\Psi'_{\pm}\rangle$  are eigenstates of the Zeeman term and are characterized by the polarization  $\langle \Psi'_{\pm} | S_{\parallel} | \Psi'_{\pm} \rangle = \pm 1$  for  $\Delta_z > \Delta_{sc}$ . The polarization of these two states remains constant up to the point  $\Delta_z = \Delta_{sc}$ , at which the gap is closed at the edges and the topological phase transition occurs. Decreasing the Zeeman term further, the spin polarization of these two states flip, acquiring a new value  $\langle \Psi'_{\pm} | S_{\parallel} | \Psi'_{\pm} \rangle = \mp 1$ . At the same time, no gap closing occurs at the edges  $s = 1, 3$ . As a consequence, the expectation value of  $S_{\parallel}$  grows smoothly as a function of the ratio  $\Delta_z/\Delta_{sc}$  without flipping its sign. Hence, the parallel component of the spin polarization changes sign only on two  $m_s \neq 0$  edges of the system as one goes through the topological phase transition and it acquires the quadrupolar structure only in the topological phase but not in the trivial one (see SM [76]). The expectation values of perpendicular components of the spin polarization are zero. This feature allows one to unambiguously identify the topological phase transition occurring in such a system.

These analytical predictions in low-energy approximation are confirmed by a numerical study of  $\mathcal{H}'$ , presented in Fig. 4, where we calculate the current through the spin-polarized STM tip (see SM [76]). When  $\Gamma > 0$ , we find that the expectation values of  $S_{\parallel}$  are always positive along the two  $y$ -edges and are positive (negative) when  $\Delta_z < \Delta_{sc}$  ( $\Delta_z > \Delta_{sc}$ ) along the two  $x$ -edges. When  $\Gamma < 0$ , the description in terms of  $\mathcal{H}'_{\text{eff},s}$  breaks down and the bulk signal dominates over the edge signal. As expected, the perpendicular components of the spin polarization is found to be negligibly small everywhere except at the system corners. We have also checked that the proposed feature is stable against weak disorder.

*Conclusions.* In this work, we analyzed the spin polarization of two-dimensional topological superconductors as a signature indicating topological phases. In particular, we showed that a spin-polarized STM can be used to determine the topological phase diagram in two types of second-order topological superconductors (SOTSCs) with broken time-reversal symmetry. In SOTSCs, which host a pair of corner states, the distinguishing feature of the topological phase is the quadrupolar structure of the spin polarization perpendicular to the Zeeman field. Similarly, in SOTSCs with two pairs of corner states, the spin polarization parallel to the Zeeman field acquires such a quadrupolar structure only in the topological phase. This probe can be used in conjunction with the usual experimental protocols, such as the state tomography and the measurement of the differential conductance, to verify the topological nature of bound states and serves as an additional independent signature of the topological phase transition.

*Acknowledgments.* We gratefully acknowledge many useful discussions with Katharina Laubscher, Flavio Ronetti, and Ferdinand Schulz. This work was supported by the Swiss National Science Foundation, NCCR QSIT, and the Georg H. Endress foundation as well as the Deutsche Forschungsgemeinschaft via RTG 1995 and by the Deutsche Forschungsgemeinschaft (DFG, German Research Foundation) under Germany's Excellence Strategy - Cluster of Excellence Matter and Light for

Quantum Computing (ML4Q) EXC 2004/1 - 390534769. This project received funding from the European Union's Horizon 2020 research and innovation program (ERC Starting Grant, grant agreement No 757725). We acknowledge support from the Max Planck-New York City Center for Non-Equilibrium Quantum Phenomena. Simulations were performed with computing resources granted by RWTH Aachen University under projects rwth0498, rwth0563, rwth0564 and rwth0593.

- 
- <sup>1</sup> C. L. Kane and E. J. Mele, Phys. Rev. Lett. **95**, 226801 (2005).
- <sup>2</sup> C. L. Kane and E. J. Mele, Phys. Rev. Lett. **95**, 146802 (2005).
- <sup>3</sup> B. A. Bernevig, T. L. Hughes, and S. Zhang, Science **314**, 5806 (2006).
- <sup>4</sup> M. Z. Hasan and C. L. Kane, Rev. Mod. Phys. **82**, 3045 (2010).
- <sup>5</sup> X.-L. Qi and S.-C. Zhang, Rev. Mod. Phys. **83**, 1057 (2011).
- <sup>6</sup> M. Sato and Y. Ando, Rep. Prog. Phys. **80**, 076501 (2017).
- <sup>7</sup> J. Wang and S.-C. Zhang, Nat. Mat. **16**, 1062-1067 (2017).
- <sup>8</sup> X.-G. Wen, Rev. Mod. Phys. **89**, 41004 (2017).
- <sup>9</sup> M. H. Freedman, A. Kitaev, M. J. Larsen, and Z. Wang, Bull. Amer. Math. Soc. **40**, 31 (2003).
- <sup>10</sup> A. Kitaev, Annals Phys. **303**, 2 (2003).
- <sup>11</sup> A. Stern and N. H. Lindner, Science **339**, 6124 (2013).
- <sup>12</sup> W. A. Benalcazar, B. A. Bernevig, and T. L. Hughes, Science **357**, 6346 (2017).
- <sup>13</sup> W. A. Benalcazar, B. A. Bernevig, and T. L. Hughes, Phys. Rev. B **96**, 245115 (2017).
- <sup>14</sup> Z. Song, Z. Fang, and C. Fang, Phys. Rev. Lett. **119**, 246402 (2017).
- <sup>15</sup> J. Langbehn, Y. Peng, L. Trifunovic, F. von Oppen, and P. W. Brouwer, Phys. Rev. Lett. **119**, 246401 (2017).
- <sup>16</sup> C. W. Peterson, W. A. Benalcazar, T. L. Hughes, and G. Bahl, Nature **555**, 346 (2018).
- <sup>17</sup> S. Imhof, C. Berger, F. Bayer, J. Brehm, L. W. Molenkamp, T. Kiessling, F. Schindler, C. H. Lee, M. Greiter, T. Neupert, and R. Thomale, Nat. Phys. **14**, 925 (2018).
- <sup>18</sup> S. Mittal, V. V. Orre, G. Zhu, M. A. Gorlach, A. Poddubny, and M. Hafezi, Nat. Photon. **10**, 1038 (2019).
- <sup>19</sup> X.-D. Chen, W.-M. Deng, F.-L. Shi, F.-L. Zhao, M. Chen, and J.-W. Dong, Phys. Rev. Lett. **122**, 233902 (2019).
- <sup>20</sup> A. E. Hassan, F. K. Kunst, A. Moritz, G. Andler, E. J. Bergholtz, and M. Bourennane, Nat. Photon. **13**, 697 (2019).
- <sup>21</sup> M. Serra-Garcia, V. Peri, R. Süsstrunk, O. R. Bilal, T. Larsen, L. G. Villanueva, and S. D. Huber, Nature **555**, 342 (2018).
- <sup>22</sup> H. Xue, Y. Yang, F. Gao, Y. Chong, and B. Zhang, Nature Materials **18**, 108 (2019).
- <sup>23</sup> F. Schindler, A. M. Cook, M. G. Vergniory, Z. Wang, S. S. P. Parkin, B. A. Bernevig, and T. Neupert, Science Advances **4**, 6 (2018).
- <sup>24</sup> F. Schindler, Z. Wang, M. G. Vergniory, A. M. Cook, A. Murani, S. Sengupta, A. Y. Kasumov, R. Deblock, S. Jeon, I. Drozdov, H. Bouchiat, S. Guéron, A. Yazdani, B. A. Bernevig, and T. Neupert, Nature Physics **14**, 918 (2018).
- <sup>25</sup> X. Ni, M. Weiner, A. Alú, and A. B. Khanikaev, Nature Materials **18**, 113 (2019).
- <sup>26</sup> X. Zhang, B.-Y. Xie, H.-F. Wang, X. Xu, Y. Tian, J.-H. Jiang, M.-H. Lu, Y.-F. Chen, Nat. Comm. **10**, 5331 (2019).
- <sup>27</sup> K. Shiozaki and M. Sato, Phys. Rev. B **90**, 165114 (2014).
- <sup>28</sup> M. Geier, L. Trifunovic, M. Hoskam, and P. W. Brouwer, Phys. Rev. B **97**, 205135 (2018).
- <sup>29</sup> E. Khalaf, Phys. Rev. B **97**, 205136 (2018).
- <sup>30</sup> L. Trifunovic and P. W. Brouwer, arXiv:2003.01144.
- <sup>31</sup> X. Zhu, Phys. Rev. B **97**, 205134 (2018).
- <sup>32</sup> Y. Volpez, D. Loss, and J. Klinovaja, Phys. Rev. Lett. **122**, 126402 (2019).
- <sup>33</sup> K. Laubscher, D. Loss, and J. Klinovaja, Phys. Rev. Research **1**, 032017 (2019).
- <sup>34</sup> J. Ahn and B.-J. Yang, Phys. Rev. Research **2**, 012060(R) (2020).
- <sup>35</sup> Y. Wang, M. Lin, and T. L. Hughes, Phys. Rev. B **98**, 165144 (2018).
- <sup>36</sup> T. Liu, J. J. He, and F. Nori, Phys. Rev. B **98**, 245413 (2018).
- <sup>37</sup> S. Franca, D. V. Efremov, and I. C. Fulga, Phys. Rev. B **100**, 075415 (2019).
- <sup>38</sup> Z. Yan, Phys. Rev. B **100**, 205406 (2019).
- <sup>39</sup> R.-X. Zhang, W. S. Cole, X. Wu, and S. Das Sarma, Phys. Rev. Lett. **123**, 167001 (2019).
- <sup>40</sup> X. Zhu, Phys. Rev. Lett. **122**, 236401 (2019).
- <sup>41</sup> K. Laubscher, D. Loss, and J. Klinovaja, Phys. Rev. Research **2**, 013330 (2020).
- <sup>42</sup> X. Wu, X. Liu, R. Thomale, C.-X. Liu, arXiv:1905.10648.
- <sup>43</sup> Y.-J. Wu, J. Hou, Y.-M. Li, X.-W. Luo, and C. Zhang, arXiv:1905.08896.
- <sup>44</sup> S.-B. Zhang, A. Calzona, and B. Trauzettel, arXiv:2003.04053.
- <sup>45</sup> Z. Yan, F. Song, and Z. Wang, Phys. Rev. Lett. **121**, 096803 (2018).
- <sup>46</sup> Q. Wang, C.-C. Liu, Y.-M. Lu, and F. Zhang, Phys. Rev. Lett. **121**, 186801 (2018).
- <sup>47</sup> C.-H. Hsu, P. Stano, J. Klinovaja, and D. Loss, Phys. Rev. Lett. **121**, 196801 (2018).
- <sup>48</sup> L. Chen, B. Liu, G. Xu, X. Liu, arXiv:1909.10402.
- <sup>49</sup> Y.-T. Hsu, W. S. Cole, R.-X. Zhang, and J. D. Sau, arXiv:1904.06361.
- <sup>50</sup> R. Zitko, J. S. Lim, R. López, and R. Aguado, Phys. Rev. B **91**, 045441 (2015).
- <sup>51</sup> E. Prada, P. San-Jose, M. W. A. de Moor, A. Geresdi, E. J. H. Lee, J. Klinovaja, D. Loss, J. Nygard, R. Aguado, and L. P. Kouwenhoven, arXiv:1911.04512.
- <sup>52</sup> C. Reeg, O. Dmytruk, D. Chevallier, D. Loss, and J. Klinovaja, Phys. Rev. B **98**, 245407 (2018).

- <sup>53</sup> A. Ptok, A. Kobiaka, and T. Domanski, *Phys. Rev. B* **96**, 195430 (2017).
- <sup>54</sup> F. Setiawan, C.-X. Liu, J. D. Sau, and S. Das Sarma, *Phys. Rev. B* **96**, 184520 (2017).
- <sup>55</sup> C. Moore, T. D. Stanescu, and S. Tewari, *Phys. Rev. B* **97**, 165302 (2018).
- <sup>56</sup> A. Vuik, B. Nijholt, A. R. Akhmerov, and M. Wimmer, *SciPost Phys.* **7**, 061 (2019).
- <sup>57</sup> J. Avila, F. Penaranda, E. Prada, P. San-Jose, and R. Aguado, *Communications Physics* **2**, 133 (2019).
- <sup>58</sup> E. B. Hansen, J. Danon, and K. Flensberg, *Phys. Rev. B* **97**, 041411 (2018).
- <sup>59</sup> F. Penaranda, R. Aguado, P. San-Jose, and E. Prada, *Phys. Rev. B* **98**, 235406 (2018).
- <sup>60</sup> G. Kells, D. Meidan, and P. W. Brouwer, *Phys. Rev. B* **86**, 100503 (2012).
- <sup>61</sup> C. Fleckenstein, F. Dominguez, N. Traverso Ziani, and B. Trauzettel, *Phys. Rev. B* **97**, 155425 (2018).
- <sup>62</sup> C. Jünger, R. Delagrangé, D. Chevallier, S. Lehmann, K.A. Dick, C. Thelander, J. Klinovaja, D. Loss, A. Baumgartner, and C. Schönenberger, *Phys. Rev. Lett.* **125**, 017701 (2020).
- <sup>63</sup> D. J. Alspaugh, D. E. Sheehy, M. O. Goerbig, and P. Simon, *Phys. Rev. Research* **2**, 023146 (2020).
- <sup>64</sup> S.-B. Zhang and B. Trauzettel, *Phys. Rev. Research* **2**, 012018 (2020).
- <sup>65</sup> P. Szumniak, D. Chevallier, D. Loss, and J. Klinovaja, *Phys. Rev. B* **96**, 041401(R) (2017).
- <sup>66</sup> M. Serina, D. Loss, and J. Klinovaja, *Phys. Rev. B* **98**, 035419 (2018).
- <sup>67</sup> M. Thakurathi, D. Chevallier, D. Loss, J. Klinovaja, *Phys. Rev. Research* **2**, 023197 (2020).
- <sup>68</sup> N. Müller, D. M. Kennes, J. Klinovaja, D. Loss, and H. Schoeller, *Phys. Rev. B* **101**, 155417 (2020).
- <sup>69</sup> C. Jozwiak, J. A. Sobota, K. Gotlieb, A. F. Kemper, C. R. Rotundu, R. J. Birgeneau, Z. Hussain, D.-H. Lee, Z.-X. Shen, and A. Lanzara, *Nature Com.*, **7**, 13143 (2016).
- <sup>70</sup> S. Jeon, Y. Xie, J. Li, Z. Wang, B. A. Bernevig, and A. Yazdani, *Science* **358**, 6364 (2017).
- <sup>71</sup> B. Jäck, Y. Xie, J. Li, S. Jeon, B. A. Bernevig, and A. Yazdani, *Science* **364**, 6447 (2019).
- <sup>72</sup> H. Kim, A. Palacio-Morales, T. Posske, L. Rózsa, K. Palotás, L. Szunyogh, M. Thorwart, and R. Wiesendanger, *Science Advances* **11**, 5251 (2018).
- <sup>73</sup> M. Ruby, B. W. Heinrich, Y. Peng, F. von Oppen, and K. J. Franke, *Nano Lett.* **17**, 4473 (2017).
- <sup>74</sup> R. Jackiw and C. Rebbi, *Phys. Rev. D* **13**, 3398 (1976).
- <sup>75</sup> R. Jackiw and J. Schrieffer, *Nucl. Phys. B* **190**, 253 (1981).
- <sup>76</sup> See Supplemental Material at ... for (1) microscopic details of the models; (2) details on the numerical methods; (3) details on the analytical calculations of the edge states and the spin polarization; (4) a study of the quadrupolar moment across the phase transition and (5) the stability of the quadrupolar features against external perturbations.
- <sup>77</sup> J. Nilsson, A. R. Akhmerov, and C. W. J. Beenakker, *Phys. Rev. Lett.* **101**, 120403 (2008).
- <sup>78</sup> L. Fu and C. L. Kane, *Phys. Rev. B* **79**, 161408(R) (2009).
- <sup>79</sup> R. M. Lutchyn, J. D. Sau, and S. Das Sarma, *Phys. Rev. Lett.* **105**, 077001 (2010).
- <sup>80</sup> Y. Oreg, G. Refael, and F. von Oppen, *Phys. Rev. Lett.* **105**, 177002 (2010).
- <sup>81</sup> J. Alicea *Phys. Rev. B* **81**, 125318 (2010).
- <sup>82</sup> M. König, S. Wiedmann, C. Brüne, A. Roth, H. Buhmann, L. W. Molenkamp, X. Qi, S. Zhang, *Science* **318**, 5851 (2007).
- <sup>83</sup> A. Roth, C. Brüne, H. Buhmann, L. W. Molenkamp, J. Maciejko, X. L. Qi, and S. C. Zhang, *Science* **325**, 294 (2009).
- <sup>84</sup> C. Liu, T. L. Hughes, X. L. Qi, K. Wang, and S. C. Zhang, *Phys. Rev. Lett.* **100**, 236601 (2008).
- <sup>85</sup> C. L. Kane, R. Mukhopadhyay, and T. C. Lubensky, *Phys. Rev. Lett.* **88**, 036401 (2002).
- <sup>86</sup> J. C. Y. Teo and C. L. Kane, *Phys. Rev. B* **89**, 085101 (2014).
- <sup>87</sup> D. Chevallier, P. Szumniak, S. Hoffman, D. Loss, and J. Klinovaja, *Phys. Rev. B* **97**, 045404 (2018).
- <sup>88</sup> D. Chevallier and J. Klinovaja, *Phys. Rev. B* **94**, 035417 (2016).
- <sup>89</sup> M. M. Maska and T. Domanski, *Scientific Reports* **7**, 16193 (2017).
- <sup>90</sup> J. Klinovaja and D. Loss, *Phys. Rev. B* **86**, 085408 (2012).
- <sup>91</sup> S. B. Zhang, Y. Y. Zhang, and S. Q. Shen, *Phys. Rev. B* **90**, 115305 (2014).
- <sup>92</sup> R. Skolasinski, D. I. Pikulin, J. Alicea, and M. Wimmer, *Phys. Rev. B* **98**, 201404(R) (2018).
- <sup>93</sup> C. Li, S. Zhang, and S. Shen, *Phys. Rev. B* **97**, 045420 (2018).
- <sup>94</sup> F. Schulz, K. Plekhanov, D. Loss, and J. Klinovaja, arXiv:2004.10623.

# Supplemental Material: Quadrupole spin polarization as signature of second-order topological superconductors

Kirill Plekhanov<sup>1</sup>, Niclas Müller<sup>2</sup>, Yanick Volpez<sup>1</sup>, Dante M. Kennes<sup>2</sup>, Herbert Schoeller<sup>2</sup>, Daniel Loss<sup>1</sup>, and Jelena Klinovaja<sup>1</sup>

<sup>1</sup> *Department of Physics, University of Basel, Klingelbergstrasse 82, CH-4056 Basel, Switzerland*

<sup>2</sup> *Institut für Theorie der Statistischen Physik, RWTH Aachen, 52056 Aachen, Germany and JARA - Fundamentals of Future Information Technology*

## S1. Microscopic details of the models

In this section, we provide microscopic details on the Hamiltonians  $\mathcal{H}_0$  and  $\mathcal{H}'_0$  considered in the main text of the manuscript. We also describe possible venues for an experimental realization of corresponding physical systems.

Firstly, we consider the Hamiltonian

$$\mathcal{H}_0(\mathbf{k}) = 2t [2 - \cos(k_x a) - \cos(k_y a)] \eta_z - \mu_0 \eta_z + \Gamma \eta_z \tau_x + \alpha [\sin(k_y a) \sigma_x - \sin(k_x a) \eta_z \sigma_y] \tau_z + \Delta_{\text{sc}} \eta_y \sigma_y \tau_z \quad (\text{S1})$$

from Eq. (1) of the main text. This Hamiltonian was first introduced in Ref. [32], where it was used to describe a system composed of two Rashba layers that are tunnel coupled to each other with an amplitude  $\Gamma$ . Here,  $t$  is the term proportional to the kinetic energy of the electrons, which is the same in both layers. Moreover, each layer is assumed to have Rashba spin-orbit interactions with an amplitude  $\alpha$  of opposite signs. In what follows, we consider  $t, \alpha > 0$ . The chemical potential  $\mu_0$  is tuned to the spin-orbit crossing point at  $\mathbf{k} = 0$ . Finally, the system is coupled to a 2D  $s$ -wave superconducting Josephson junction with a phase factor of  $\pi$ , inducing a superconducting pairing  $\Delta_{\text{sc}}$  via the proximity effect. The Pauli matrices  $\eta_j$  act on the particle-hole space,  $\sigma_j$  – on the spin space, and  $\tau_j$  – on the space associated with two Rashba layers. The lattice spacing is denoted by  $a$ .

Secondly, we consider the Hamiltonian

$$\mathcal{H}'_0(\mathbf{k}) = \{ \Gamma - 2t_x [1 - \cos(k_x a)] - 2t_y [1 - \cos(k_y a)] \} \eta_z \tau_z - \mu_0 \eta_z + [\alpha_x \sin(k_x a) \sigma_z \tau_x - \alpha_y \sin(k_y a) \eta_z \tau_y] + \Delta_{\text{sc}} \eta_y \sigma_y \quad (\text{S2})$$

from Eq. (5) of the main text. In the regime when  $t_x \sim t_y$  and  $\alpha_x \sim \alpha_y$ ,  $\mathcal{H}'_0$  can be seen as a modified version of the BHZ Hamiltonian [3], where we neglect the usual kinetic term (which does not have any effect on the topological description), but where we take into account the anisotropy effect in the  $xy$ -plane. In this case, the degrees of freedom associated with  $\tau_j$  correspond to electron/hole orbitals. The hopping amplitudes  $t_x$  and  $t_y$  describe anti-symmetric components of the kinetic term, while  $\alpha_x$  and  $\alpha_y$  are the spin-orbit interaction amplitudes. In what follows, all these parameters are assumed to be strictly greater than zero. The parameter  $\Gamma$  is responsible for the topological phase transition between a trivial insulator and the TI. In a quantum well experimental setup,  $\Gamma$  depends on the thickness of the quantum well [82–84].

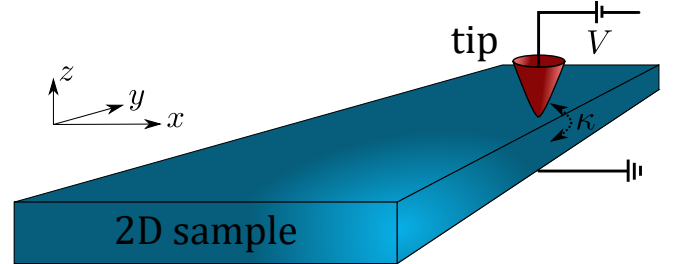


FIG. S1. Schematic representation of the setup. The spin-polarized STM tip biased at voltage  $V$  is brought close to the 2D sample which realizes a SOTSC. The current measured using STM allows one to probe the topological phase diagram of the SOTSC.

In addition to the BHZ model,  $\mathcal{H}'_0$  can also be generated using a coupled wire construction [85, 86] in a strongly anisotropic regime with  $t_y \ll t_x$ ,  $\alpha_y \ll \alpha_x$ . In this case,  $t_x$  and  $\alpha_x$  correspond to the kinetic and Rashba terms along the wire direction, while  $t_y$  and  $\alpha_y$  correspond to the inter-wire couplings, which are much smaller in amplitude.

## S2. Numerical methods

In an STM measurement, the tip of the microscope, biased at the voltage  $V$ , is brought close to the sample. This results in a current flowing through the tip into the sample, the amplitude of which depends on the LDOS of the sample and on the overlap between the wavefunctions of the sample and the tip. Hence, if the tip is spin-polarized, the STM measurement will provide additional information on the spin polarization of the sample. Moreover, the voltage difference between the sample and the tip determines how many eigenstates contribute to the current. We note that, alternatively, one can use spin-polarized quantum dots [87–89], however, they are less mobile.

In our work, we model the STM measurement and perform numerical simulations using the Keldysh formalism [68]. To do this calculation, we consider the following setup consisting of two parts: the sample, corresponding to a 2D SOTSC, and the STM tip, are described by the Hamiltonians  $\mathcal{H}_{\text{sam}}$  and  $\mathcal{H}_{\text{tip}}$ , respectively. The STM tip is tunnel coupled to the sample with an amplitude denoted by  $\kappa$  (see Fig. S1). The sample is simulated on

a square lattice, and the tunneling between the tip and the sample is assumed to occur locally at one given site of the lattice, depending on the position of the tip. The effect of the applied voltage  $V$  induces the difference of the chemical potential  $eV$  between the tip and the sample, with  $e$  – the electron charge. The influence of the tip is encoded in the induced self-energy which dresses the bare Green's function of the sample. The resulting time-dependent current flowing from the probe reservoir into the sample at time  $t$  can be expressed using the Keldysh formalism as

$$J(t) = -e \int dt' \text{Tr} \{ \Sigma^R(t, t') G^<(t', t) - G^<(t, t') \Sigma^A(t', t) \}, \quad (\text{S3})$$

where  $\Sigma^{R/A}$  are the retarded/advanced self-energies of the STM tip,  $G^{\lessgtr}$  are the fully dressed greater/lesser Green's functions of the sample, and  $e$  is the electron charge which is assumed to be equal to one. In the wide band limit and at the equilibrium, the above expression simplifies to

$$J = e \text{Tr} \int \frac{d\omega}{2\pi} \Sigma^<(\omega) G^R(\omega) \Sigma^<(\omega) G^A(\omega). \quad (\text{S4})$$

In the main part of the manuscript, we mostly focus on the features of the sample close to the boundary, and show that they provide an alternative way to probe the topological phase transition in some classes of SOTSCs. We also present how the result of such a calculation varies as a function of the tip polarization and the sample Hamiltonian  $\mathcal{H}_{\text{sam}}$ , describing different types of SOTSCs. In the section ‘‘Quadrupolar structure of  $\langle S_{\perp} \rangle$ ’’ the sample Hamiltonian is taken to be  $\mathcal{H}$ , while in the section ‘‘Quadrupolar structure of  $\langle S_{\parallel} \rangle$ ’’ it is  $\mathcal{H}'$ .

### S3. Analytical calculation of edge states and spin polarization

In this section, we provide details on the analytical calculation of the wavefunctions associated with helical states in both models considered in the main text. We also study the effect of the perturbations, which are added to the models in order to gap out the helical modes, and calculate the expectation values of the spin operators to deduce their spin polarization.

#### A. SOTSC with two corner states

##### 1. Properties of the $s = 0$ edge

We start with the model described by the Hamiltonian  $\mathcal{H}_0$  from Eq. (1) [32]. We fix the chemical potential as  $\mu_0 = 0$  and take the lattice spacing  $a$  to be equal to one. First, we consider the  $s = 0$  edge localized at  $y = 0$ . We focus on the physics at the point  $k_x = 0$ , which describes

the solutions uniform along the  $x$  axis. We also linearize the resulting problem around the Fermi momenta  $k_{F,i} = 0$  and  $k_{F,e} = \arctan(\alpha/t)$  [90]. In order to do this, we switch to the basis of slowly varying left and right movers

$$\begin{aligned} \tilde{\psi}_{\uparrow 1} &= \tilde{L}_{\uparrow 1} e^{-ik_{F,e}y} + \tilde{R}_{\uparrow 1}, & \tilde{\psi}_{\downarrow 1} &= \tilde{L}_{\downarrow 1} + \tilde{R}_{\downarrow 1} e^{ik_{F,e}y}, \\ \tilde{\psi}_{\uparrow \bar{1}} &= \tilde{L}_{\uparrow \bar{1}} + \tilde{R}_{\uparrow \bar{1}} e^{ik_{F,e}y}, & \tilde{\psi}_{\downarrow \bar{1}} &= \tilde{L}_{\downarrow \bar{1}} e^{-ik_{F,e}y} + \tilde{R}_{\downarrow \bar{1}}, \end{aligned} \quad (\text{S5})$$

defined such that  $\tilde{\sigma} = \uparrow, \downarrow$  denotes the spin projection onto the  $x$  axis. In this new basis, the linearized Hamiltonian reduces to

$$\tilde{\mathcal{H}}_0 = \alpha k_y \delta_z + \Gamma \eta_z (\tau_x \delta_x - \tau_y \delta_y \tilde{\sigma}_z) \eta_z / 2 + \Delta_{\text{sc}} \eta_y \tilde{\sigma}_y \tau_z \delta_x, \quad (\text{S6})$$

where the Pauli matrices  $\delta_j$  act on the space of left and right movers. The obtained problem can be solved by substituting  $k_y = -i\partial_y$  and imposing vanishing boundary condition at  $y = 0$ . We find that in the region  $\Gamma > \Delta_{\text{sc}}$ , the system admits two zero-energy solutions described by the following wavefunctions:

$$\begin{aligned} \Psi_{0,+}^0(y) &= \frac{1}{\mathcal{N}} (f_1, g_1, f_1^*, g_1^*, f_{\bar{1}}, g_{\bar{1}}, f_{\bar{1}}^*, g_{\bar{1}}^*)^T, \\ \Psi_{0,-}^0(y) &= \frac{1}{\mathcal{N}} (g_{\bar{1}}^*, -f_{\bar{1}}^*, g_1, -f_1, g_{\bar{1}}^*, -f_{\bar{1}}^*, g_{\bar{1}}, -f_{\bar{1}})^T, \end{aligned} \quad (\text{S7})$$

where we used Eq. (S5) to go back to the original basis  $(\psi_{\uparrow 1}, \psi_{\downarrow 1}, \psi_{\uparrow \bar{1}}^\dagger, \psi_{\downarrow \bar{1}}^\dagger, \psi_{\uparrow \bar{1}}, \psi_{\downarrow \bar{1}}, \psi_{\uparrow \bar{1}}^\dagger, \psi_{\downarrow \bar{1}}^\dagger)$ . Here  $\mathcal{N}$  is the normalization constant, and the functions  $f_\tau$  and  $g_\tau$  are expressed as

$$f_1 = g_{\bar{1}} = -if_{\bar{1}}^* = -ig_1^* = e^{-y/\xi_i} - e^{ik_{F,e}y} e^{-y/\xi_e}, \quad (\text{S8})$$

with  $\xi_i = \alpha/(\Gamma - \Delta_{\text{sc}})$  and  $\xi_e = \alpha/\Delta_{\text{sc}}$ . As expected from the Kramers partner of gapless helical modes in a helical topological superconductor, the two obtained solutions satisfy  $T|\Psi_{0,\pm}^0\rangle = \pm|\Psi_{0,\mp}^0\rangle$  and  $P|\Psi_{0,\pm}^0\rangle = |\Psi_{0,\pm}^0\rangle$ , where  $P = \eta_x K$  is the particle-hole symmetry operator.

By using the particular form of the solutions at  $k_x = 0$ , obtained in Eq. (S7), we can now include perturbatively the omitted Zeeman term as well as the first order kinetic term in  $k_x$ . To begin with, we express the term linear in  $k_x$  as

$$\begin{aligned} \langle \Psi_{0,\pm}^0 | -\alpha k_x \eta_z \sigma_y \tau_z | \Psi_{0,\pm}^0 \rangle &= \pm v_F k_x, \\ \langle \Psi_{0,+}^0 | -\alpha k_x \eta_z \sigma_y \tau_z | \Psi_{0,-}^0 \rangle &= 0, \end{aligned} \quad (\text{S9})$$

where  $v_F = \alpha\Delta/\Gamma$  is the Fermi velocity of the edge modes. Similarly, the two components of the Zeeman term can be expressed as

$$\begin{aligned} \langle \Psi_{0,\pm}^0 | \Delta_z \cos(\theta_z) \eta_z \sigma_x | \Psi_{0,\pm}^0 \rangle &= 0, \\ \langle \Psi_{0,+}^0 | \Delta_z \cos(\theta_z) \eta_z \sigma_x | \Psi_{0,-}^0 \rangle &= i\Delta_z \cos(\theta_z), \\ \langle \Psi_{0,\pm}^0 | \Delta_z \sin(\theta_z) \sigma_y | \Psi_{0,\pm}^0 \rangle &= 0, \\ \langle \Psi_{0,+}^0 | \Delta_z \sin(\theta_z) \sigma_y | \Psi_{0,-}^0 \rangle &= 0. \end{aligned} \quad (\text{S10})$$

Combining these two results, we recover the effective Jackiw-Rebbi Hamiltonian

$$\mathcal{H}_{\text{eff},0}(k_x) = v_F k_x \rho_z - \Delta_z \cos(\theta_z) \rho_y, \quad (\text{S11})$$

which describes the low-energy physics of the edge  $s = 0$ .

## 2. Remaining edges and quadrupolar structure of the spin polarization

Next, we obtain similar results for the three remaining edges of the system by using the rotational symmetry of the Hamiltonian  $\mathcal{H}_0$ . The rotational symmetry operator can be explicitly written down as  $U_{\text{rot}}(\theta) = \exp[i\theta(L_z + S_z)]$ , where  $L_z = -i(x\partial_y - y\partial_x)$  and  $S_z = \eta_z \sigma_z / 2$  are the  $z$  component of the orbital momentum and the spin, respectively. The non-perturbed Hamiltonian satisfies  $U_{\text{rot}}(\theta) \mathcal{H}_0(\mathbf{k}) U_{\text{rot}}^{-1}(\theta) = \mathcal{H}_0(\mathbf{k})$ . As a consequence, the expression of the states at the three remaining edges can be obtained by using  $|\Psi_{0,\pm}^s\rangle = U_{\text{rot}}(\theta_s) |\Psi_{0,\pm}^0\rangle$ , where  $\theta_s = s\pi/2$ . The Zeeman term is not invariant under the rotation symmetry transformation:

$$U_{\text{rot}}^{-1}(\theta) \mathcal{H}_z U_{\text{rot}}(\theta) = \Delta_z [\cos(\theta - \theta_z) \eta_z \sigma_x + \sin(\theta - \theta_z) \sigma_y]. \quad (\text{S12})$$

Combining this with the results of Eq. (S10), we deduce that the gap opened by the Zeeman term on the edge  $s$  can be expressed as  $m_s = \Delta_z \cos(\theta_z - \theta_s)$ . We note that this gap, indeed, satisfies  $m_0 = -m_2$  and  $m_1 = -m_3$ , as required by the inversion symmetry.

Finally, we calculate the expectation values of the spin operators  $S_{\parallel} = \cos(\theta_z) \eta_z \sigma_x + \sin(\theta_z) \sigma_y$  and  $S_{\perp} = \cos(\theta_z) \sigma_y - \sin(\theta_z) \eta_z \sigma_x$  in the basis of the eigenstates of the effective Hamiltonian  $\mathcal{H}_{\text{eff},s}$  at  $k_s = 0$ . These states diagonalize  $\mathcal{H}_z$  and, hence, can be found as  $|\Phi_{\pm}^s\rangle = (|\Psi_{0,+}^s\rangle \mp i |\Psi_{0,-}^s\rangle) / \sqrt{2}$ , in correspondence to the eigenvalues  $\pm m_s$ . By ordering these states according to their eigenvalues, we recover the two states  $|\Psi_{\pm}^s\rangle$  of the main text corresponding to the eigenvalues  $\pm |m_s|$ . Trivially, the parallel component of the spin polarization of these states is equal to

$$\langle \Psi_{\pm}^s | S_{\parallel} | \Psi_{\pm}^s \rangle = \pm |m_s| / \Delta_z = \pm |\cos(\theta_z - \theta_s)|. \quad (\text{S13})$$

In order to calculate the perpendicular in-plane component of the polarization, we make use of the fact that

$$\begin{aligned} \langle \Phi_{\pm}^s | S_{\perp} | \Phi_{\pm}^s \rangle &= \langle \Phi_{\pm}^s | U_{\text{rot}}(\pi/2) S_{\parallel} U_{\text{rot}}^{-1}(\pi/2) | \Phi_{\pm}^s \rangle \\ &= \langle \Phi_{\pm}^{s-1} | S_{\parallel} | \Phi_{\pm}^{s-1} \rangle = \pm m_{s-1} / \Delta_z. \end{aligned} \quad (\text{S14})$$

Hence, once the states on the  $s$ -edge are ordered, we obtain

$$\begin{aligned} \langle \Psi_{\pm}^s | S_{\perp} | \Psi_{\pm}^s \rangle &= \pm \text{sgn}(m_s) m_{s-1} / \Delta_z \\ &= \pm \text{sgn}(m_s) \cos(\theta_z - \theta_{s-1}). \end{aligned} \quad (\text{S15})$$

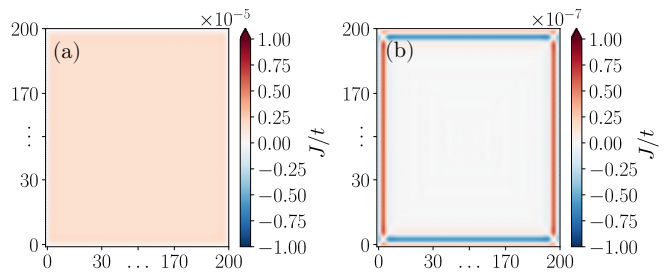


FIG. S2. Numerical calculation of the current  $J$  through the spin-polarized STM tip in the topologically trivial phase of  $\mathcal{H}$  with  $\Gamma = 0.25\Delta_{\text{sc}} = 0.06t$ . The polarization of the STM is chosen to be (a) parallel to the Zeeman field and (b) perpendicular to the Zeeman field. The remaining parameters are the same as in Fig. 2. The quadrupolar structure of  $J$  is absent for the parallel component of the spin polarization. We observe the reminiscence of the quadrupolar structure for the perpendicular component, however the resulting current is several orders of magnitude smaller than in the topological phase (see Fig. 2)

These theoretical arguments are confirmed by numerical simulations of a current flowing through the spin-polarized tip in an STM measurement setup, see Fig. 2 for a topological phase with  $\Gamma = 1.75\Delta_{\text{sc}}$  and Fig. S2 for a topologically trivial phase with  $\Gamma = 0.25\Delta_{\text{sc}}$ . We find that, in the topological phase, the current is strongest at the edges. When the tip polarization is parallel to the direction of the Zeeman field, the current is approximately uniform and negative along the entire boundary of the systems. However, when the tip polarization is perpendicular to the Zeeman field (but still lying in the  $xy$  plane), the current acquires a quadrupolar structure. In the trivial phase, only bulk states contribute to the current and the resulting signal is a few orders of magnitude smaller than in the topological phase.

## B. SOTSC with four corner states

### 1. Properties of the $s = 0$ edge

In the second part of this section, we study the low-energy physics of the model described by the Hamiltonian  $\mathcal{H}'_0(\mathbf{k})$ , see Eq. (5). Similarly to Section S3 A, we start by considering the  $s = 0$  edge at  $k_x = 0$ , corresponding to a uniform solution localized at  $y = 0$ . We fix  $\mu_0 = 0$  and set  $a = 1$ . Moreover, for a moment, we neglect the superconducting pairing term  $\Delta_{\text{sc}}$ , which we will include later perturbatively. This allows us to focus only on electron or hole parts of the spectrum. To describe the electron part of the spectrum, we choose the basis  $(\psi_{\uparrow 1}, \psi_{\downarrow 1}, \psi_{\uparrow \bar{1}}, \psi_{\downarrow \bar{1}})$ . We expand the Hamiltonian up to second order in  $k_y$  around  $k_y = 0$ , which leads us to

$$\mathcal{H}'_0(k_x = 0, k_y) \approx (\Gamma - t_y k_y^2) \tau_z - \alpha_y k_y \tau_y. \quad (\text{S16})$$

We proceed by substituting  $k_y = -i\partial_y$  and looking for zero-energy solutions of the resulting equation. After imposing vanishing boundary condition at  $y = 0$ , we find two exponentially decaying solutions of the form

$$\begin{aligned}\Psi_{0,+}^{\prime 0}(y) &= \frac{e^{-y/\xi_+} - e^{-y/\xi_-}}{\mathcal{N}} [1, 0, 1, 0]^T, \\ \Psi_{0,-}^{\prime 0}(y) &= \frac{e^{-y/\xi_+} - e^{-y/\xi_-}}{\mathcal{N}} [0, 1, 0, 1]^T,\end{aligned}\quad (\text{S17})$$

where  $\mathcal{N}$  is the normalization constant. Such solutions exist only for  $\Gamma > 0$ , and the parameters  $\xi_{\pm}$  are given by

$$\xi_{\pm}^{-1} = \frac{1}{2t_y} \left( \alpha_y \pm \sqrt{\alpha_y^2 - 4\Gamma t_y} \right). \quad (\text{S18})$$

The two states are related by the time-reversal symmetry such that  $T|\Psi_{0,\pm}^{\prime 0}\rangle = \pm|\Psi_{0,\mp}^{\prime 0}\rangle$ . We note that the Hamiltonian defined in Eq. (S16) does not contain Pauli matrices describing the spin space. Hence, the spin quantization axis of the states  $|\Psi_{0,\pm}^{\prime 0}\rangle$  could be also chosen arbitrarily. Here, we decided to choose the form of the two states as in Eq. (S17), such that it agrees with the choice of the spin quantization axis from the main text and the notation for the edge  $s = 1$ .

Using the expression of the two states at  $k_x = 0$ , we calculate the expectation values of the Zeeman term and the kinetic term linear in  $k_x$ . For the latter term, we obtain

$$\begin{aligned}\langle \Psi_{0,\pm}^{\prime 0} | \alpha_x k_x \sigma_z \tau_x | \Psi_{0,\pm}^{\prime 0} \rangle &= \pm v_F k_x, \\ \langle \Psi_{0,+}^{\prime 0} | \alpha_x k_x \sigma_z \tau_x | \Psi_{0,-}^{\prime 0} \rangle &= 0,\end{aligned}\quad (\text{S19})$$

where  $v_F = \alpha_x$ . The expectation values of the Zeeman term are

$$\begin{aligned}\langle \Psi_{0,\pm}^{\prime 0} | \Delta_z \sigma_x | \Psi_{0,\pm}^{\prime 0} \rangle &= 0, \\ \langle \Psi_{0,+}^{\prime 0} | \Delta_z \sigma_x | \Psi_{0,-}^{\prime 0} \rangle &= \Delta_z.\end{aligned}\quad (\text{S20})$$

In order to take into account the superconducting  $s$ -wave pairing, we introduce a pair of states  $|\Psi_{0,\pm}^{\prime 0*}\rangle$ , which correspond to the particle-hole partners of the states  $|\Psi_{0,\pm}^{\prime 0}\rangle$ . These states belong to the second block of the Nambu space. This allows us to write the effective low-energy Hamiltonian describing the system boundary as

$$\mathcal{H}'_{\text{eff},0}(k_x) = v_F k_x \rho_z + \Delta_z \eta_z \rho_x + \Delta_{\text{sc}} \eta_y \rho_y. \quad (\text{S21})$$

Here,  $\eta_j$  acts in the particle-hole space and  $\rho_j$  – in the space of the two edge states. We note that we recover Eq. (7) from the main text with  $m_0 = \Delta_z$ . Next, we focus again on the physics at momentum  $k_x = 0$  and diagonalize  $\mathcal{H}'_{\text{eff},0}$ . It is easy to see that the two eigenstates corresponding to the two lowest magnitude eigenvalues  $\pm(\Delta_z - \Delta_{\text{sc}})$  can be expressed as

$$\begin{aligned}|\Phi_+^{\prime 0}\rangle &= \frac{1}{2} (|\Psi_{0,+}^{\prime 0}\rangle + |\Psi_{0,-}^{\prime 0}\rangle - |\Psi_{0,+}^{\prime 0*}\rangle + |\Psi_{0,-}^{\prime 0*}\rangle), \\ |\Phi_-^{\prime 0}\rangle &= \frac{1}{2} (|\Psi_{0,+}^{\prime 0}\rangle - |\Psi_{0,-}^{\prime 0}\rangle - |\Psi_{0,+}^{\prime 0*}\rangle - |\Psi_{0,-}^{\prime 0*}\rangle).\end{aligned}\quad (\text{S22})$$

From this, we deduce that

$$\langle \Phi_{\pm}^{\prime 0} | S_{\parallel} | \Phi_{\pm}^{\prime 0} \rangle = \pm 1, \quad \langle \Phi_{\pm}^{\prime 0} | S_{\perp} | \Phi_{\pm}^{\prime 0} \rangle = 0, \quad (\text{S23})$$

where  $S_{\parallel} = \eta_z \sigma_x$  and  $S_{\perp} = \sigma_y$  are the parallel and perpendicular components of the spin polarization, respectively. Finally, we sort the states according to their energies, from negative to positive, to arrive at  $|\Psi_{\pm}^{\prime 0}\rangle$ . The initial ordering of the states  $|\Phi_{\pm}^{\prime 0}\rangle$  is correct in the regime  $\Delta_z > \Delta_{\text{sc}}$ , but has to be changed when  $\Delta_z < \Delta_{\text{sc}}$ . Hence, we deduce that in the basis of new, correctly ordered states, the expectation values of the spin polarization become equal to  $\langle \Psi_{\pm}^{\prime 0} | S_{\parallel} | \Psi_{\pm}^{\prime 0} \rangle = \pm 1$  when  $\Delta_z > \Delta_{\text{sc}}$  and  $\langle \Psi_{\pm}^{\prime 0} | S_{\parallel} | \Psi_{\pm}^{\prime 0} \rangle = \mp 1$  otherwise.

## 2. Properties of the $s = 1$ edge

In the same way as for the edge  $s = 0$ , we do the calculations on the second non-equivalent edge of the system denoted by  $s = 1$  by considering the physics at  $k_y = 0$ . After expanding the Hamiltonian  $\mathcal{H}'_0(\mathbf{k})$  [see Eq. (5)] to second order in  $k_x$ , we obtain

$$\mathcal{H}'_0(k_x, k_y = 0) \approx (\Gamma - t_x k_x^2) \tau_z + \alpha_x k_x \sigma_z \tau_x. \quad (\text{S24})$$

By substituting  $k_x = -i\partial_x$  and imposing vanishing boundary condition at  $x = 0$ , we find two exponentially decaying solutions at zero energy which have the form

$$\begin{aligned}\Psi_{0,+}^{\prime 1}(x) &= \frac{e^{-x/\xi_+} - e^{-x/\xi_-}}{\mathcal{N}} [1, 0, i, 0]^T, \\ \Psi_{0,-}^{\prime 1}(x) &= \frac{e^{-x/\xi_+} - e^{-x/\xi_-}}{\mathcal{N}} [0, 1, 0, -i]^T,\end{aligned}\quad (\text{S25})$$

where the parameters  $\xi_{\pm}$  are given by

$$\xi_{\pm}^{-1} = \frac{1}{2t_x} \left( \alpha_x \pm \sqrt{\alpha_x^2 - 4\Gamma t_x} \right). \quad (\text{S26})$$

Similarly, we find that the kinetic term is diagonal in the basis of the two states, with

$$\begin{aligned}\langle \Psi_{0,\pm}^{\prime 1} | \alpha_y k_y \tau_y | \Psi_{0,\pm}^{\prime 1} \rangle &= \pm v_F k_y, \\ \langle \Psi_{0,+}^{\prime 1} | \alpha_y k_y \tau_y | \Psi_{0,-}^{\prime 1} \rangle &= 0,\end{aligned}\quad (\text{S27})$$

where  $v_F = \alpha_y$ . However, unlike on the edge  $s = 0$ , here we find that all expectation values of the Zeeman term are exactly zero

$$\begin{aligned}\langle \Psi_{0,\pm}^{\prime 1} | \Delta_z \sigma_x | \Psi_{0,\pm}^{\prime 1} \rangle &= 0, \\ \langle \Psi_{0,+}^{\prime 1} | \Delta_z \sigma_x | \Psi_{0,-}^{\prime 1} \rangle &= 0.\end{aligned}\quad (\text{S28})$$

We note that this feature is independent of the orientation of the Zeeman field and is crucial to generate four corner states. Taking into account the proximity induced superconductivity effect, we can now express the effective low-energy Hamiltonian as

$$\mathcal{H}'_{\text{eff},1}(k_y) = v_F k_y \rho_z + \Delta_{\text{sc}} \eta_y \rho_y, \quad (\text{S29})$$

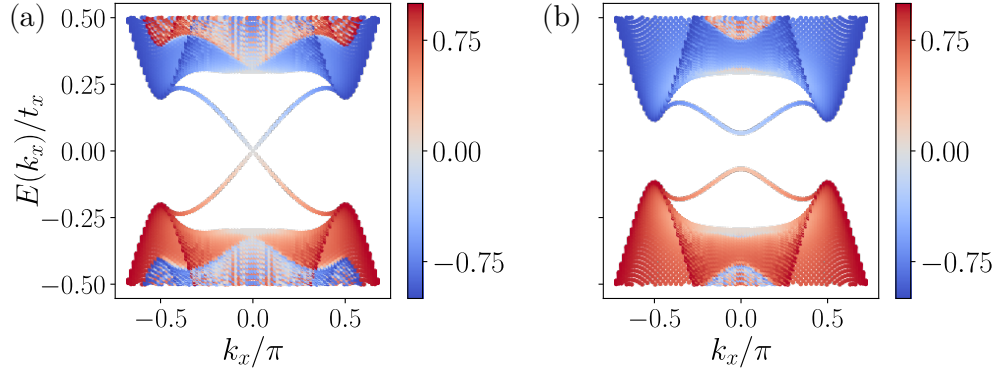


FIG. S3. Numerical calculation of the spin polarization of the eigenstates of  $\mathcal{H}'$  in a geometry with OBC (PBC) along the  $x$  ( $y$ ) axis. The color corresponds to  $\langle \Psi_j(k_y) | S_{\parallel} | \Psi_j(k_y) \rangle$ , where  $|\Psi_j(k_y)\rangle$  is the  $j$ -th eigenstate of  $\mathcal{H}'$ . (a) When  $\Delta_{sc} = 0$ , the edge spectrum remains gapless and the spin polarization of the states is zero at  $k_y = 0$ . (b) When  $\Delta_{sc} = 0.1t_x$ , the edge spectrum is gapped out and the spin polarization becomes non-zero even at  $k_y = 0$ . Nevertheless, the sign of the spin polarization remains the same as in (a). All the remaining parameters are the same as in Fig. 3(b).

which we immediately identify with the topologically trivial regime.

In order to find the spin polarization of the edge states along the edge  $s = 1$ , we solve the problem by

explicitly taking into account the kinetic and Zeeman terms. The new problem is described by the Hamiltonian  $\mathcal{H}'_0(k_x, k_y) + \Delta_z \sigma_x$ . To lowest order in  $k_y$  and  $\Delta_z$ , the corresponding solutions can be expressed as

$$\begin{aligned}
 \tilde{\Psi}'_{0,+}(x) &= \sum_{\lambda=\pm} \lambda \frac{e^{-x/\xi_{1,\lambda}}}{\mathcal{N}} [1 + f_{1,\lambda}, 1 + f_{1,\lambda}, i(1 - f_{1,\lambda}), i(f_{1,\lambda} - 1)]^T \\
 &\quad + \sum_{\lambda=\pm} \lambda \frac{e^{-x/\xi_{2,\lambda}}}{\mathcal{N}} [1 + f_{2,\lambda}, -(1 + f_{2,\lambda}), i(1 - f_{2,\lambda}), i(1 - f_{2,\lambda})]^T, \\
 \tilde{\Psi}'_{0,-}(x) &= \sum_{\lambda=\pm} \lambda \frac{e^{-x/\xi_{1,\lambda}}}{\mathcal{N}} [1 + f_{1,\lambda}, 1 + f_{1,\lambda}, i(1 - f_{1,\lambda}), i(f_{1,\lambda} - 1)]^T \\
 &\quad - \sum_{\lambda=\pm} \lambda \frac{e^{-x/\xi_{2,\lambda}}}{\mathcal{N}} [1 + f_{2,\lambda}, -(1 + f_{2,\lambda}), i(1 - f_{2,\lambda}), i(1 - f_{2,\lambda})]^T,
 \end{aligned} \tag{S30}$$

with  $f_{j,\pm} = (-1)^j \xi_{j,\pm} \alpha_y k_y / (2\alpha_x)$ ,  $\tilde{\xi}_{1,\pm}^{-1} = (\alpha_x \pm \sqrt{\alpha_x^2 - 4(\Gamma + \Delta_z)t_x}) / (2t_x)$ , and  $\tilde{\xi}_{2,\pm}^{-1} = (\alpha_x \pm \sqrt{\alpha_x^2 - 4(\Gamma - \Delta_z)t_x}) / (2t_x)$ . We verify that the new solutions reproduce correctly Eq. (S25) in the limit  $\Delta_z = 0$  and  $k_y = 0$ . We also find that under the

effect of the Zeeman field, the condition of the existence of the edge modes is modified to  $\Gamma > |\Delta_z|$ , such that the topological phase becomes smaller when the Zeeman field increases. Moreover, the polarization of the edge states is defined by the following expression:

$$\langle \tilde{\Psi}'_{0,\pm} | S_{\parallel} | \tilde{\Psi}'_{0,\pm} \rangle = \pm 4 \frac{\sum_j \Re [f_{j,+} \xi_{j,+} + f_{j,-} \xi_{j,-} - 4f_{j,+} f_{j,-} / (\xi_{j,+}^{-1} + \xi_{j,-}^{-1*})]}{\sum_j \Re [\xi_{j,+}^{-1} + \xi_{j,-}^{-1*}]}. \tag{S31}$$

As expected, the parallel component of the spin polar-

ization is zero for  $\Delta_z = 0$  independently of the value of

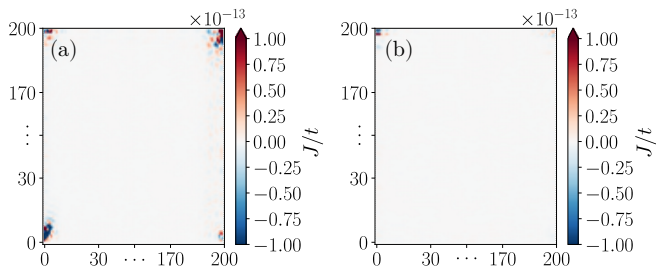


FIG. S4. Numerical calculation of the current  $J$  through the STM tip that is polarized perpendicularly to the Zeeman field along the  $y$  axis (a) in the topological phase with  $\Delta_z = 1.75\Delta_{sc}$  and (b) in the trivial phase with  $\Delta_z = 0.25\Delta_{sc}$ . The remaining parameters of the simulations are the same as in Fig. 4. The perpendicular component of the spin polarization is trivially zero everywhere except at the four corners of the system.

$k_y$ . The same is true for  $k_y = 0$ , independently of the value of  $\Delta_z$ . These features are confirmed numerically in Fig. S3(a), where we calculate the spin polarization of the eigenstates of  $\mathcal{H}'$  in a geometry with the OBC (PBC) along the  $x$  ( $y$ ) axis as a function of the momentum  $k_y$ . Moreover, we find that the spin polarization changes smoothly as a function of  $\Delta_z$ . We also note that both perpendicular components of the spin polarization are exactly zero.

If the superconducting term is taken into account, the spectrum of states  $|\Psi_{0,\pm}^1\rangle$  acquires a finite gap. Nevertheless, we expect that the spin polarization of the edge states keeps the same sign for different values of the ratio  $\Delta_z/\Delta_{sc}$  across the entire phase transition. This is confirmed by numerical calculations presented in Fig. S3(b). We also note that for  $\Delta_{sc} \neq 0$ , the edge states become spin polarized even at  $k_y = 0$ .

### 3. Quadrupolar structure of the spin polarization

Finally, by considering the effect of the inversion symmetry that maps  $\mathbf{k}$  to  $-\mathbf{k}$ , we relate the description of the edge  $s = 2$  ( $s = 3$ ) to the one of the edge  $s = 0$  ( $s = 1$ ). More specifically, we use that  $I\mathcal{H}'(\mathbf{k})I^{-1} = \mathcal{H}'(-\mathbf{k})$ , where  $I = \tau_z$ , which implies that the mass terms at opposite edges have opposite signs:  $m_0 = -m_2 = \Delta_z$  and  $m_1 = -m_3 = 0$ . This allows us to see that the total boundary of the system is composed of two pairs of effective Rashba wires forming an alternating pattern, only one of which is affected by the Zeeman field. As a result, in the topological regime  $\Delta_z > \Delta_{sc}$ , the system is described by the parallel component of the spin polarization flipping its sign from one edge to another, resulting in a quadrupolar spin structure, which can indeed be observed in Fig. 4 of the main text. Such a feature is directly associated with the emergence of MCSs and allows one to probe the topological phase transition which occurs in the

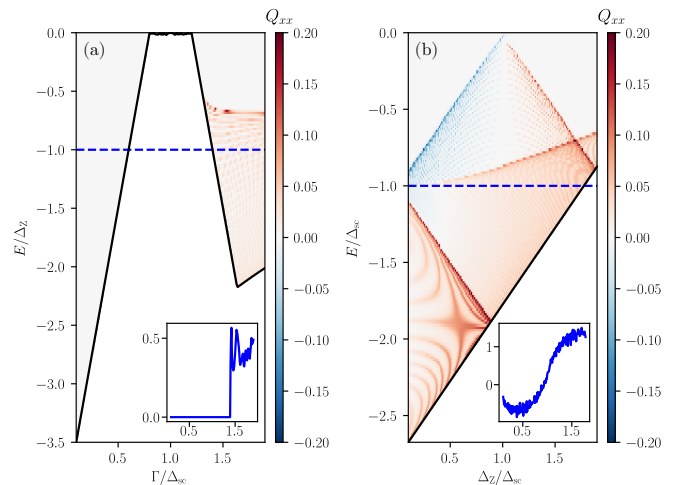


FIG. S5. Energy-resolved value of the quadrupolar moment  $Q_{xx}$  evaluated across the topological phase transition for the two models considered in the main text. Insets show the contribution summed from the blue lines up to the chemical potential. Black lines separate the contribution coming from the edges (shown) and the bulk (not shown). (a) The model is described by the Hamiltonian  $\mathcal{H}$  and  $Q_{xx}$  is calculated as a function of  $\Gamma/\Delta_{sc}$  with  $\Delta E = 0.02\Delta_z$ . All the remaining parameters are the same as in Fig. 2. The trivial (topological) phase corresponds to zero (finite) value of the quadrupolar moment. (b) The model is described by the Hamiltonian  $\mathcal{H}$  and  $Q_{xx}$  is calculated as a function of  $\Delta_z/\Delta_{sc}$  with  $\Delta E = 0.015\Delta_{sc}$ . All the remaining parameters are the same as in Fig. 4. The spin polarization of the  $x$ -edge states changes sign at the phase transition, while for  $y$ -edge states it slowly increases with  $\Delta_z$ . As a consequence, the integrated value of  $Q_{xx}$  crosses zero close to the topological phase transition point.

system. We also verify numerically (see Fig. S4) that the perpendicular components of the spin polarization are trivially zero everywhere except at the four corners of the system, where they acquire some finite value as a result of the broken translation symmetry along the edge.

## S4. Quadrupolar moment

In the main text, we demonstrated that the structure of the edge spin polarization allows one to detect the topological phase transition in SOTSCs with broken time-reversal symmetry. In particular, we found that in SOTSCs hosting a pair of MCSs at two opposite corners the sign of the spin polarization perpendicular to the Zeeman field of low-energy states changes on every edge. This feature has been denoted as quadrupolar structure of the spin polarization. Similarly, we observed that a SOTSC which hosts a MCS at each of the four corners is described by a quadrupolar structure of the spin polarization parallel to the applied Zeeman field.

Here, we further analyze the quadrupolar structure of

the spin polarization by introducing the energy-resolved quadrupolar tensor  $Q_{\mu\nu}$  associated with the STM current  $J$ . Assuming that the sample is a perfect square and by placing the origin of coordinates in the square center we can define the following quantity:

$$Q_{\mu\nu}(E) = \sum_i [2r_\mu(i)r_\nu(i) - \mathbb{I}_{\mu\nu}] J(\mathbf{r}_i, E)/N. \quad (\text{S32})$$

Here  $r_\mu(i)$  denotes the position of the site with the lattice index  $i$  and  $\mathbb{I}$  is the  $2 \times 2$  identity matrix. The sum over  $i$  runs over all the sites of the system and  $N$  denotes the total number of sites. The current  $J(\mathbf{r}_i, E)$  refers to the contribution defined in Eq. (S4) for a small window  $[E - \Delta E/2, E + \Delta E/2]$ . We calculate this quantity in both models across the phase transition. We also focus only on the diagonal component  $Q_{xx} = -Q_{yy}$  of the quadrupolar tensor with the off-diagonal components being trivially zero.

First, we consider the model presented in Section ‘‘SOTSCs with two corner states’’ [see Fig. S5(a)]. We assume that the STM tip polarization is perpendicular to the Zeeman field and calculate  $Q_{xx}$  as a function of  $\Gamma/\Delta_{\text{sc}}$ . We find that in the topologically trivial phase, the quadrupolar moment is exactly zero, since no available edge states are present in the considered energy window. In the topological phase, on the contrary,  $Q_{xx}$  is positive that can be associated with the quadrupolar structure of spin polarization at the edges.

Similarly, we consider the model presented in Section ‘‘SOTSCs with four corner states’’ with the STM tip polarization being parallel to the Zeeman field [see Fig. S5(b)]. We clearly distinguish the contribution coming from different edges: the energy of the  $x$ -edge states increases with  $\Delta_z$  until it reaches zero at the critical point  $\Delta_z = \Delta_{\text{sc}}$ , after which it starts decreasing again; a large quadrupolar moment flips sign at the phase transition. For  $\Delta_z > \Delta_{\text{sc}}$ , we also observe the emergence of edge states at lower energies, which live on the  $x$ -edge and are described by the spin polarization of an opposite sign. At the same time, the energy of the  $y$ -edge states as well as their quadrupolar moment slowly increases with  $\Delta_z$  without flipping its sign. As a result, when integrated over the energy  $E$ , the quadrupolar moment changes sign at the topological phase transition.

We notice that the precise value of  $Q_{xx}$  depends strongly on the energy  $E$ . Nevertheless, the quadrupolar structure, namely the sign change of the spin polarization on the neighboring edges of the system, is typical for topological phases close to the phase boundary. Hence, the quadrupolar structure of the spin polarization remains a prominent probe of the SOTSCs topology as long as the effective low-energy description stays valid.

Finally, we note that the quadrupolar tensor  $Q_{\mu\nu}(E)$  is less suitable for direct experimental observation as it requires integration of the current signal across the entire sample. Moreover, the values of  $Q_{\mu\nu}(E)$  depend on the sample geometry such as size and shape, as well as on the choice of coordinate origin in the definition of  $Q_{\mu\nu}$ ,

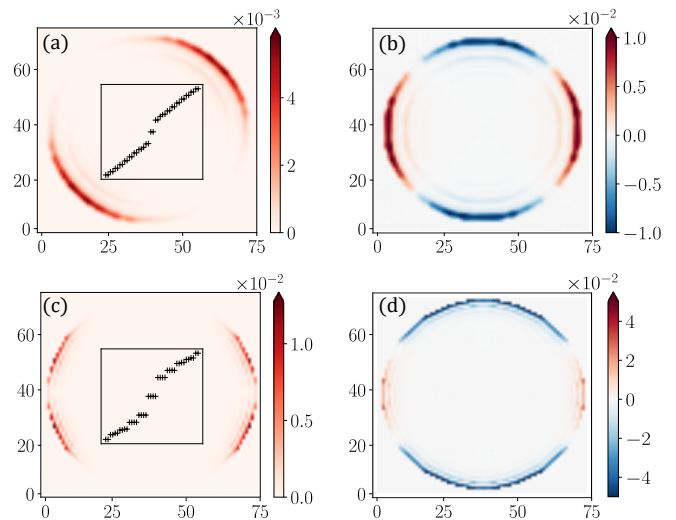


FIG. S6. (a) Numerical calculation of the MCS wavefunctions and (b) the total spin polarization of 40 states below the Fermi level in the topological phase of the system described by the Hamiltonian  $\mathcal{H}$  in a disk geometry. The parameters used are  $\Gamma = 2\Delta_{\text{sc}} = \alpha = 0.5t$ ,  $\mu_0 = 0$ ,  $\Delta_z = 0.05t$ , and  $\theta_z = \pi/4$ . (c,d) The same calculation as before but the system is now described by the Hamiltonian  $\mathcal{H}'$  with  $\Gamma = t_y = t_x$ ,  $\alpha_x = \alpha_y = 0.3t_x$ ,  $\mu_0 = 0$ , and  $\Delta_z = 2\Delta_{\text{sc}} = 0.1t_x$ . As expected, in both cases, we observe MCSs, emphasizing that the shape of the sample does not play a substantial role. The corresponding spin polarization shows the quadrupole structure.

since, in general, the total spin polarization and dipole moments are non-zero.

## S5. Stability of quadrupolar polarization

We also provide additional numerical results, demonstrating the stability of the quadrupolar polarization feature for the two SOTSC classes considered in the main text. To do this, we simulate the system in a disc geometry, which does not have any well defined edges and corners. Nevertheless, MCSs still emerge in such a geometry. Their position is unambiguously determined by the symmetries of the system, namely, the inversion symmetry  $I$  of the Hamiltonian  $\mathcal{H}$  from the section ‘‘SOTSCs with two corner states’’ and the in-plane anisotropy of the Hamiltonian  $\mathcal{H}'$  from the section ‘‘SOTSCs with four corner states’’ of the main text. In Figs. S6(a) and (b), we show that, in the model described by  $\mathcal{H}$ , two corner states emerge at two opposite extremities of the disc, aligned with the direction of the Zeeman field. The perpendicular component of the spin polarization changes sign at four equal-sized quadrants delimited by the Zeeman field vector and the vector normal to it. Similarly, in Figs. S6(c) and (d), we show that four corner states emerge in the model described by  $\mathcal{H}'$ , dividing the disk into four quadrants. The parallel component of the spin polarization has opposite signs in neighboring quadrants,

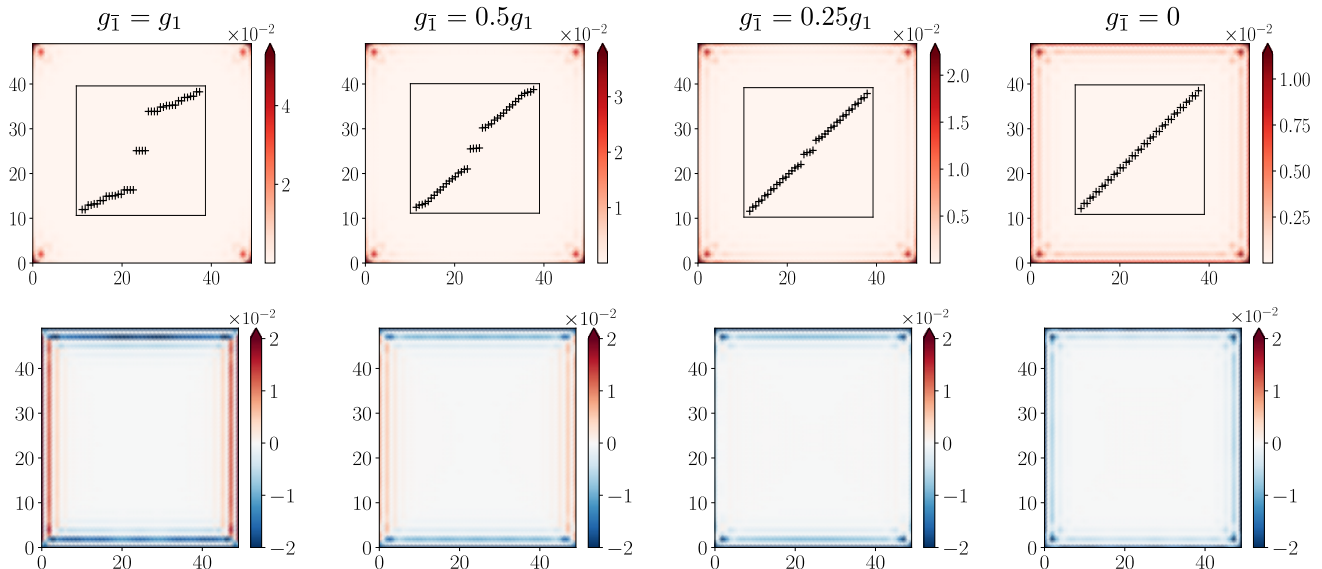


FIG. S7. (first row) Numerical calculation of the MCS wavefunctions and (second row) the total spin polarization of 40 states below the Fermi level in the topological phase of a system described by the Hamiltonian  $\mathcal{H}'$  for different values of the  $g$ -factor ratio  $g_{\bar{1}}/g_1$  (different columns). The remaining parameters are the same as in Fig. 3(b) of the main text. We confirm that the inversion symmetry between two bands, which gets broken if  $g$ -factors are different, is indeed not needed. The MCSs survive even if the  $g$ -factors are substantially different.

while the perpendicular component remains trivially zero everywhere. The size of the quadrants is determined by the ratio  $\Delta_z/\Delta_{sc}$ , such that in the limit  $\Delta_z \ll \Delta_{sc}$  the corner states merge pairwise at the top and bottom extremities of the disk.

Additionally, having in mind an experimental realization in quantum wells [82–84, 91–94] of our model with four corner states described by the Hamiltonian  $\mathcal{H}'$ , we study how the topological phase diagram and the result of the STM measurement vary as a function of  $g$ -factors

of the electron and hole bands, denoted by  $g_1$  and  $g_{\bar{1}}$ , respectively. The result of such a calculation is presented in Fig. S7. We find that the topological phase and, as a result, the quadrupolar polarization features are stable even for a strong  $g$ -factor anisotropy. However, when  $g_{\bar{1}}$  becomes of the order of  $0.25g_1$  (and vice versa), a phase transition occurs leading to the closing of the bulk gap, accompanied by the disappearance of the corner states as well as of the quadrupolar structure of the spin polarization.